Acta Oceanol. Sin., 2024, Vol. 43, No. 9, P. 26–34
https://doi.org/10.1007/s13131-024-2357-0
http://www.aosocean.com
E-mail: ocean2@hyxb.org.cn

Cold filament frontogenesis and frontolysis induced by thermal convection turbulence using large eddy simulation

Zewen Wu[1], Guojing Li[2, 3]*, Yunkai He[1]*, Jintuan Zhang[2]

[1] State Key Laboratory of Tropical Oceanography, South China Sea Institute of Oceanology, Chinese Academy of Sciences, Guangzhou 510301, China

[2] School of Architecture and Electrical Engineering, Hezhou University, Hezhou 542889, China

[3] Southern Marine Science and Engineering Guangdong Laboratory (Zhuhai), Zhuhai 519080, China

Received 16 January 2024; accepted 24 June 2024

Abstract

The frontogenetic processes of a submesoscale cold filament driven by the thermal convection turbulence are studied by a non-hydrostatic large eddy simulation. The results show that the periodic changes in the direction of the cross-filament secondary circulations are induced by the inertial oscillation. The change in the direction of the secondary circulations induces the enhancement and reduction of the horizontal temperature gradient during the former and later inertial period, which indicates that the frontogenetical processes of the cold filament include both of frontogenesis and frontolysis. The structure of the cold filament may be broken and restored by frontogenesis and frontolysis, respectively. The magnitude of the down-filament currents has a periodic variation, while its direction is unchanged with time. The coupling effect of the turbulent mixing and the frontogenesis and frontolysis gradually weakens the temperature gradient of the cold filament with time, which reduces frontogenetical intensity and enlarges the width of cold filament.

Key words: cold filament, frontogenesis, frontolysis, thermal convection turbulence, large eddy simulation

Citation: Wu Zewen, Li Guojing, He Yunkai, Zhang Jintuan. 2024. Cold filament frontogenesis and frontolysis induced by thermal convection turbulence using large eddy simulation. Acta Oceanologica Sinica, 43(9): 26–34, doi: 10.1007/s13131-024-2357-0

1 Introduction

Submesoscale motions, such as submesoscale front (the density step) and filament (the density line) currents and submesocale eddies, are the key processes in the ocean (Capet et al., 2008a, b, c; McWilliams, 2016; Zhang et al., 2021; Taylor and Thompson, 2023). The scales of submesoscale currents are O (0.1–10 km) in the horizontal direction and O (0.01–1 km) in the vertical direction (McWilliams, 2016, 2021). The boundary layer turbulence (thermal convection turbulence induced by the sea surface cooling, Langmuir turbulence induced by the wave-current interactions and shear turbulence induced by the wind forcing) is also an important process in the upper mixed layer (Skyllingstad and Denbo, 1995; McWilliams et al., 1997; Sullivan et al., 2007; Sullivan and McWilliams, 2018, 2019). The frontogenesis of the fronts and filaments may be induced by both of the mesoscale strain (Hoskin, 1982; McWilliams and Fox-Kemper, 2013) and the turbulent vertical mixing (Gula et al., 2014; McWilliams et al., 2009, 2015). The frontogenesis of the fronts and filaments created by the turbulent vertical mixing is called the turbulent thermal wind (TTW) (Gula et al., 2014; McWilliams, 2017). The TTW is a balance among the baroclinic pressure gradient, Coriolis force and turbulent vertical mixing (McWilliams et al., 2015). McWilliams et al. (2015) found that the cold filament frontogenesis induced by the turbulent vertical mixing is consistent with that caused by the mesoscale strain. The ageostrophic secondary circulations driven by the strain of the mesoscale motions or the turbulent vertical mixing are associated with the horizontal width and buoyancy gradient of the submesoscale fronts and filaments (Lapeyre et al., 2006; Boccaletti et al., 2007; Shakespeare and Tayor, 2013; Gula et al., 2014; Hamlington et al., 2014; McWilliams et al., 2015; Smith et al., 2016; Suzuki and Fox-Kemper, 2016; McWilliams, 2017, 2018; Pham and Sarkar, 2018; Sullivan and McWilliams, 2018, 2019; Barkan et al., 2019), that is, whether the ageostrophic secondary circulations are activated by the strain of the mesoscale motions or the turbulent vertical mixing depends on the intensity of the fronts and filament. The submesoscale motions impact the variation of the upper mixed layer and large-scale circulations (Lapeyre et al., 2006; Dauhajre et al., 2017; Hypolite et al., 2021; Zhang et al., 2023a), thus the studies of the submesoscale processes are used to parameterize the effect of the submesoscale motions on the large-scale processes in the general ocean circulation models (GOCMs) (Fox-Kemper et al., 2008; Bodner et al., 2023; Zhang et al., 2023b).

The theory of the TTW balance has been used to study the frontogenesis of the submesoscale fronts and filaments from Gula et al. (2014) and McWilliams et al. (2015). The frontogenesis of a dense filament induced by the turbulent vertical mixing is simulated by the regional ocean modeling system (ROMS) (McWilliams et al., 2015), the results shown that the spatial symmetry of the down- and cross-filament currents only created by

Foundation item: The National Key Research and Development Program of China under contract No. 2022YFC3103400; the National Natural Science Foundation of China under contract Nos 42076019 and 42076026; the Project supported by Southern Marine Science and Engineering Guangdong Laboratory (Zhuhai) under contract No. SML2023SP240.
*Corresponding author, E-mail: ligjhzu@163.com; heyk@scsio.ac.cn

the idealized vertical eddy viscosity can be distorted through the surface wind forcing. McWilliams (2017) diagnosed the flow fields of the fronts and filaments forced by the surface wind stress based on the TTW balance, the results indicated that the frontogenetical tendencies of the submesoscale currents associated with the TTW relation are similar to that caused the mesoscale strain-induced frontogenesis. Dauhajre et al. (2017) found that the secondary circulations subject to the strong diurnal variation of the surface heating and turbulent vertical mixing do not consist with the steady-state TTW balance. McWilliams (2018) explored the surface wave effects on the submesoscale fronts and filaments using a method of the diagnostic analysis, the results displayed that the influence of the short waves on the submesoscale frontogenesis is stronger relative to the swell waves. Crow and Taylor (2018, 2019) examined the effect of the small-scale turbulence on the evolution of the submesoscale front with the imposed viscosity and diffusivity, they found that the dominant balance is the quasi-steady TTW balance with time owing to an advection-diffusion balance in the buoyancy equation, the spreading rate is maximum for an intermediate value of the Ekman number (the depth-averaged dimensional viscosity). The above results show that the TTW balance is an important theory for studying the dynamic mechanism of the submesoscale frontogenesis in the upper mixed layer. Barkan et al. (2019) further verified the TTW balance based on an asymptotic mode of the submesoscale frontogenesis.

Large eddy simulation (LES) model is a valuable tool to explore the effect of the boundary layer turbulence on the variation in the submesoscale flow fields of the fronts and filaments, when the secondary circulations may be created by the turbulent vertical mixing (McWilliams et al., 2015; McWilliams, 2019; Yuan and Liang, 2021). For a cold filament, the thermal convection turbulence induced by the sea surface cooling causes the spatial symmetry of the secondary circulations, geostrophic currents and temperature gradients, whereas the shear turbulence caused by the wind force distorts the symmetry of submesoscale flow fields (Sullivan and McWilliams, 2018). Langmuir turbulence induced by the wave-current interactions (Leibovich, 1983) can further disrupt the symmetry of submesoscale flow fields of a cold filament (Sullivan and McWilliams, 2019). Sullivan and McWilliams (2018, 2019) also discovered that the frontogenetical evolution of a cold filament should include the onset, arrest and decay periods regardless of the force fields, while the frontogenesis intensity of a cold filament is influenced by the force fields that may create or disrupt the symmetry of the flow fields. Sullivan and McWilliams (2024) found that the magnitude of the initial horizontal buoyancy gradient and the sea surface flux plays an important role in the frontogenetical strength of the cold filament frontogenesis, but the cold filament frontolysis does not appear in their simulations.

The Coriolis effect may induce the periodic increase and decrease in the gradient of the cross-front flow for a front during the period $0 < t < \pi/f$ and $\pi/f < t < 2\pi/f$, respectively, which causes that the front frontogenesis and frontolysis occur during one inertial period (Blumen, 2000). For a cold filament frontogenesis related to the TTW relation, the upwelling jet appears near the left edge of the downwelling jet at the arrest time, when the frontogenesis processes are induced by the force of the wind stress and the wind and wave fields (McWilliams, 2017, 2018; Sullivan and McWilliams, 2018, 2019). Li et al. (2024) further found that for the frontogenesis of a cold filament associated with the TTW relation, the frontogenetical evolution caused by Langmuir turbulent includes both of the frontogenesis and the frontolysis due to the inertial oscillation, that is, the change in the direction of the secondary circulations and the enhancement and reduction of the temperature gradient occur during one inertial period. Furthermore, when a cold filament frontogenesis is created by the thermal convection turbulence, the upwelling jet does not appear on the left or right edge of the downwelling jet (Sullivan and McWilliams, 2018). Hence, this raises a question: for a submesoscale cold filament, whether the direction of the secondary circulations induced by the thermal convection turbulence also periodically change with time due to the inertial oscillation?

The remainder of this paper is organized as follows: Section 2 describes briefly the LES model and an idealized simulation case, and Section 3 presents the evolution in the direction and amplitude of the temperature field and the submesoscale currents with time. A summary of the findings is given in Section 4.

2 Large eddy simulation and an idealized case

2.1 *Large eddy simulation*

The dynamics of the upper mixed layer, including the thermal convection turbulence and the submesoscale currents, is assumed to be described by a conventional LES model (Skyllingstad and Denbo, 1995; McWilliams et al., 1997; Skyllingstad and Samelson, 2012; Sullivan and McWilliams, 2018). The LES equation set with the system rotation and stable stratification is given by

$$\frac{\partial u_i}{\partial x_i} = 0, \tag{1}$$

$$\frac{\partial u_i}{\partial t} + \frac{\partial u_i u_j}{\partial x_j} = -\frac{\partial P}{\partial x_i} - \frac{\partial \tau_{ij}}{\partial x_j} - \xi_{ijk} u_j f_k - \delta_{i3} g \frac{\rho}{\rho_0}, \tag{2}$$

$$\frac{\partial e}{\partial t} + u_j \frac{\partial e}{\partial x_j} = S_{\mathrm{sgs}} + B_{\mathrm{sgs}} - \varepsilon + D_{\mathrm{sgs}}, \tag{3}$$

$$\frac{\partial T}{\partial t} + \frac{\partial u_j T}{\partial x_j} + \frac{\partial \tau_{Tj}}{\partial x_j} = 0, \tag{4}$$

where x_i ($i = 1, 2, 3$) is the Cartesian coordinate, u_i is the resolved velocity components in the x_i direction, t is the time, f_k is the Coriolis parameter, $P = p/\rho_0 + 2e/3$ is the modified pressure, p is the pressure, e is the turbulent kinetic energy of the sub-grid-scale, $\tau_{ij} = \nu_t S_{ij}$ is the momentum flux of the sub-grid-scale, ν_t is the turbulent eddy viscosity, $S_{ij} = 1/2\left(\partial u_i/\partial x_j + \partial u_j/\partial x_i\right)$ is the strain tensor of the resolved velocities, ξ_{ijk} is the standard antisymmetric tensor, δ_{i3} is the Kronecker delta, $\rho = \rho[1 - \alpha(T - T_0)]$ is density, ρ_0 is the reference density, α is the thermal expansion coefficient, g is the gravity acceleration, $S_{\mathrm{sgs}} = -\tau_{ij} S_{ij}$ is the shear production of the sub-grid-scale, $B_{\mathrm{sgs}} = g\tau_{Tk}/T_0$ is the buoyancy production of the sub-grid-scale, T_0 is the reference temperature, $\varepsilon = 0.93e^{3/2}/\Delta$ ($\Delta = \sqrt[3]{\Delta x \Delta y \Delta z}$, where Δx, Δy, and Δz are the grid spacings) is the dissipation rate, $D_{\mathrm{SGS}} = \partial(2\nu_t \partial e/\partial x_i)/\partial x_i$ is the diffusion production of the sub-grid-scale, T is the resolved temperature, $\tau_{Tj} = -\nu_T \partial T/\partial x_i$ is the heat flux of the sub-grid-scale, and ν_T is the turbulent eddy diffusivity. The terms $\nu_t = 0.1le^{1/2}$ and $\nu_T = (1 + 2l/\Delta)\nu_t$ are suggested by Moeng (1984) and Sullivan et al. (1994), where $l = \Delta$ within the upper mixed layer and $l = 0.76e^{1/2}(g/T_0)(\partial T/\partial z)$ in the thermocline.

2.2 *Idealized filament structures*

The two-dimension (2-D) (x-z plane) model of an idealized dense filament is set in the temperature field of the simulation domain. The buoyancy (b) is calculated based on the resolved temperature (T) by $\rho = \rho_0 [1 - \alpha (T - T_0)]$ and $b = g(\rho_0 - \rho)/\rho_0$. The filament axis is alignment with the y direction. Hence, x, y, and z are referred to as the cross-filament, the down-filament and the vertical directions. The simulation domain is (L_x, L_y, H) = (12, 4.5, –0.25) km and the grid number is (N_x, N_y, N_z) = (8 192, 3 072, 256). The horizontal grid spacing is $\Delta x = \Delta y = 1.46$ m and the vertical grid spacing is $\Delta z = 0.98$ m. The grid scale in this study can resolve both of the thermal convective turbulence and the submesoscale currents (Wang, 2011; Sullivan and Patton, 2011; Hamlington et al., 2014; Smith et al., 2016; Suzuki and Fox-Kemper, 2016). The grid number is more than 6.4 billion, which means that the simulation needs the great amount of the calculation due to the non-hydrostatic approximation.

We follow the cold filament structure of McWilliams (2017, 2018), the buoyancy field ($b(x,z)$) for a 2-D filament is idealized as

$$b(x,z) = b_0 + N_b^2 (z + H) + N_0^2/2\{(1+\Gamma) z - (1-\Gamma)\{h(x) + \lambda^{-1}\log_{10}\{\cosh[\lambda(z + h(x))]\}\}\}, \tag{5}$$

where b_0 is the buoyancy in the centerline of the cross-filament axis; H is the depth of the computational domain; $h(x)$ is the change in the depth of the upper mixed layer with the x-coordinate; N_0^2 is the square of the buoyancy frequency for the interior stratification; N_b^2 is a weak background minimum stratification, that is, $0 < N_b^2 \ll N_0^2$; Γ ($0 \ll \Gamma \ll 1$) is the coefficient for the fractional reduction of the upper mixed layer stratification compared to the interior stratification N_0^2. The vertical scale of the transition between these two regimes λ^{-1} appears around the base of the upper mixed layer $z = -h(x)$. In the rigid-lid model, $z = 0$ is the sea surface.

For a cold filament, the depth of the upper mixed layer is given by

$$h(x) = h_0 + \delta h_0 \exp\left[-\left(\frac{x}{W_D}\right)^2\right], \tag{6}$$

where $x = 0$ is the center of the filament, W_D is half-width of the filament, h_0 is the depth of the upper mixed layer, and δh_0 is an increase in the depth of the filament center.

The constants employed in the above formulas are

$$\begin{cases} H = 250 \text{ m}, \\ N_0^2 = 3.4 \times 10^{-5} \text{ s}^{-2}, \\ \Gamma = 0.002\,5, \\ b_0 = 6.4 \times 10^{-3} \text{ m/s}^2, \\ N_b^2 = 1.0 \times 10^{-7} \text{ s}^{-2}, \\ W_D = 1.5 \text{ km}, \\ h_0 = 60 \text{ m}, \\ \delta h_0 = 15 \text{ m}, \\ \lambda^{-1} = 3 \text{ m}. \end{cases} \tag{7}$$

The above definitions create an initial cold filament in the cross-filament (x-z) plane. The width of the cold filament is $2W_D = 3$ km. The LES directly solves the temperature equation. The reference temperature is $T_0 = 13$℃ at $z = -H$ and the thermal expansion coefficient is $\alpha \approx 2.0 \times 10^{-4}$ K^{-1}, thus the surface temperature difference in the filament centerline is $(T_{s0} - T_0) = 3.3$℃ and the temperature variation is $\delta T_0 = 0.25$℃ (McWilliams, 2017).

2.3 *Forcing fields*

We follow method of Sullivan and McWilliams (2018), a kinematic heat flux $Q_* = 2.38 \times 10^{-5}$ K/(m·s) is imposed on the sea surface. The vertical velocity scale related to the thermal convection is $w_* = (\alpha h_0 Q_*)^{1/3} = 6.6 \times 10^{-3}$ m/s (Deardorff, 1972). The Coriolis parameter $f = 1.25 \times 10^{-4}$ s^{-1} in this simulation. Figure 1 shows the clod filament structures, the background submesoscale currents diagnosed by the TTW balance, the sea surface heat flux and the Coriolis parameter.

2.4 *Basic boundary conditions and numerical method*

The surface cooling imposes on the sea surface ($z = 0$ m). The

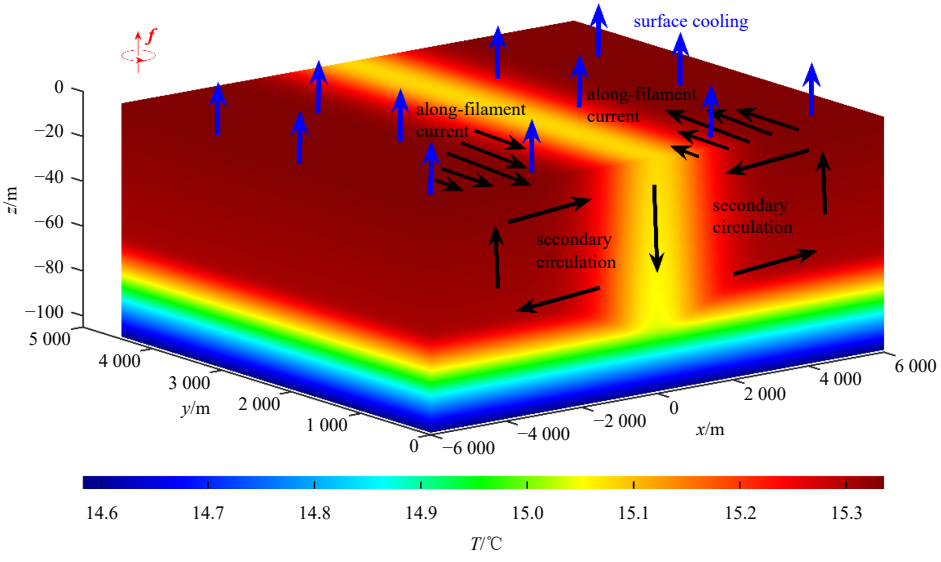

Fig. 1. Structures of the submesoscale cold filament, the background submesoscale currents diagnosed by the turbulent thermal wind balance, the surface cooling, and the Coriolis parameter. The black arrow indicates the direction of the submesoscale currents and the blue arrow indicates the direction of sea surface heat flux and the Coriolis parameter (f) is indicated by the red arrow.

stress-free conditions are used on the bottom boundary ($z = -H$) (Haney et al., 2015). The periodic boundary conditions are used in the horizontal (x-y) planes. The spatial discretization is the second-order finite differences in the vertical direction and the pseudospectral method in the horizontal directions (Sullivan and McWilliams, 2019). The time integral is advanced by the third-order Runge-Kutta scheme (RK3).

2.5 *Simulation steps*

Firstly, the simulation is integrated for an inertial period $t = 2\pi/f \approx 14$ h with a horizontal homogeneous upper mixed layer, which generates the well-developed thermal convection turbulence. The pre-existing turbulence may suppress the large-scale meandering and long-time disintegration of a cold filament caused by the baroclinic instabilities (Kaminski and Smyth, 2019; Sullivan and McWilliams, 2019). Secondly, an idealized 2-D (x-z plane) filament is introduced into the last volume of the fully developed convection turbulence and the simulation is integrated forward about 1.35 h, the ageostrophic secondary circulation fully develops. Thirdly, an idealized 2-D (x-z plane) cold filament is again introduced into the last volume of the fully developed ageostrophic secondary circulation to avoid the effect of the possible buoyancy field slumping in the former integral time period. Finally, the subsequent integral time references the third step as $t = 0$ h and the simulation of the frontogenetical process affected by the surface cooling is freely integrated forward 27.54 h.

3 Results

3.1 *Overview of frontogenetical activity*

The submesoscale flow fields of the cold filament are projected onto the cross-filament (x-z) plane with the spatial average in the along-filament (y) direction, which may reduce the random errors and highlight the main structures of the submesoscale flow fields (Skyllingstad and Samelson, 2012; Hamlington et al., 2014; Suzuki and Fox-Kemper, 2016; Sullivan and McWilliams, 2018, 2019; Verma et al., 2019). Hereafter the spatial average flow fields in the down-filament (y) direction are indicated by the angle bracket $\langle\cdot\rangle$.

The peak value vertical velocity $\langle w\rangle_{\mathrm{p}}$ (the subscript p represents "peak") in the middle of the upper mixed layer ($z \approx -30$ m) is a key indicator for the cold filament frontogenesis (McWilliams et al., 2015). The evolution of the peak vertical velocity is shown in Fig. 2. The change in the magnitude and direction of the peak vertical velocity is periodic with time and the variation period is an inertial period ($2\pi/f = 14$ h), which may hint that the direction of the secondary circulation may periodically change due to the inertial oscillation (Li et al., 2024). Thus, the frontogenetical processes of the cold filament caused by the thermal convection turbulence should include both of the frontogenesis and the frontolysis. Furthermore, the amplitude of the negative peak vertical velocity is much larger than the positive peak vertical velocity, which implies that the intensity of the frontogenesis is much stronger than the frontolysis. Furthermore, when the negative/positive $\langle w\rangle_{\mathrm{p}}$ reaches the maximum absolute value, the frontogenesis/frontolysis is arrest (McWilliams et al., 2015; Li et al., 2024).

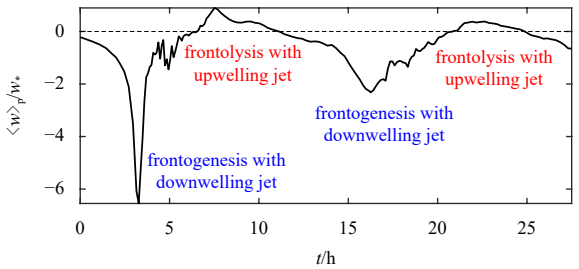

Fig. 2. Time variation of the normalized average peak vertical velocity $\langle w\rangle_{\mathrm{p}}$ in the middle of the upper mixed layer ($z \approx -30$ m). The negative and positive $\langle w\rangle_{\mathrm{p}}$ represent the frontogenesis and frontolysis.

The cross-filament profiles of the cross-filament velocity $\langle u\rangle$ in a near-surface layer of the depth (0 m > z > –5 m) and the vertical velocity $\langle w\rangle$ in a middle-layer of the depth (–28 m > z > –32 m) are an important informative metric for the frontogenesis and frontolysis of the cold filament induced by the direction of a tow-cell secondary circulation $\langle u, w\rangle$ (McWilliams et al., 2015, Sullivan and McWilliams, 2018; Li et al., 2024). Figure 3 shows the cross-filament profiles of the cross-filament velocity and the vertical velocity at the time stamp of the first frontogenesis/frontolysis arrest $t = 3.27$ h/7.51 h (Fig. 2). For $t = 3.27$ h corresponding to the first frontogenesis arrest (Fig. 2), the cross-filament velocity is positive/negative on the left/right side of the cold filament (Fig. 3a) and the vertical velocity is negative in the filament center (Fig. 3b), which is the pattern of secondary circulation inducing the cold filament frontogenesis (McWilliams et al., 2009). For $t = 7.51$ h corresponding to the first frontolysis arrest (Fig. 2), the cross-filament velocity is negative/positive on the left/right side of cold filament (Fig. 3c) and the vertical velocity is positive in the filament center (Fig. 3d), which is the structure of the secondary circulation creating the cold filament frontolysis. Moreover, the gradient of the cross-filament velocity in the range of the cold core shown in Fig. 3a is much steeper relative to that shown in Fig. 3c, the amplitude of the cross-filament and vertical velocities displayed in Fig. 3b are much larger than that displayed in Fig. 3d. This result suggests that the frontogenesis sharps the gradient of the cross-filament velocity, the frontolysis weakens the gradient of the cross-filament velocity, and the intensity of the frontogenesis is stronger compared to the frontolysis.

3.2 *Flow patterns of cold filament at the first arrest time of frontogenesis and frontolysis*

The submesoscale flow patterns of the cold filament in the x-z plane can indicate the cold filament frontogenesis and frontolysis (Blumen, 2000; Sullivan and McWilliams, 2019). Figure 4 shows the submesoscale flow fields at $t = 3.27$ h corresponding to the time stamp of the first frontogenesis arrest (Fig. 2). The width of the cold filament above/below $z = -22$ m is narrower/wider relative to the initial state (Fig. 4a). The reason is that the secondary circulations $\langle u, w\rangle$ induce the warm/cold water advecting toward/away from the cold core above/below $z = -22$ m (Fig. 4b) and the downwelling jet in the range of cold core transporting the warm water to the deeper depth (Fig. 4d). The down-filament velocity $\langle v\rangle$ is negative/positive on the left/right flank of the cold filament (Fig. 4c). The basic structures of submesoscale flow fields for the cold filament (Fig. 4) are similar to the previous studies of McWilliams et al. (2015), McWilliams (2017, 2018), Sullivan and McWilliams (2018, 2019), and Li et al. (2024). Furthermore, the significant upwelling currents appear near the left and right edges of the downwelling jet (Fig. 4d), then the upwelling currents will gradually develop into the upwelling jet in the range of the cold core.

Figure 5 shows the submesoscale flow fields at $t = 7.51$ h cor-

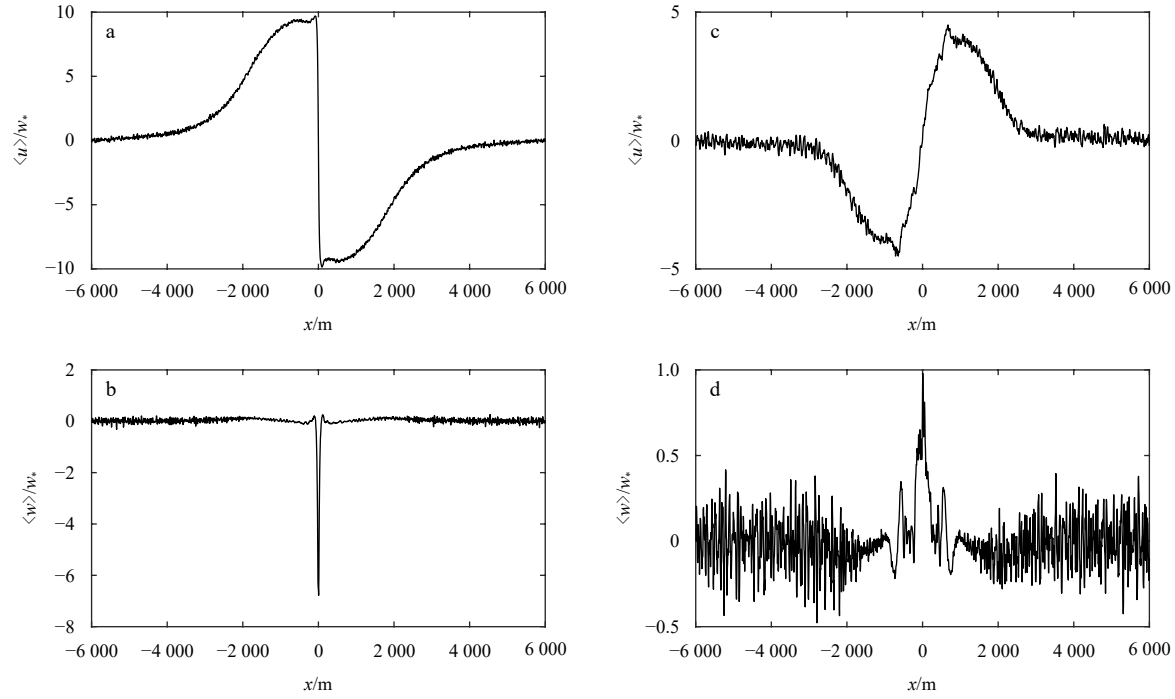

Fig. 3. Cross-filament profiles for the normalized cross-filament velocity $\langle u\rangle$ at t = 3.27 h in a near-surface layer of the depth (0 m > z > –5 m) (a), the normalized vertical velocity $\langle w\rangle$ at t = 3.27 h in a middle-layer of the depth (–28 m > z > –32 m) (b), the normalized cross-filament velocity $\langle u\rangle$ at t = 7.51 h in a near-surface layer of the depth (0 m > z > –5 m) (c), and the vertical velocity $\langle w\rangle$ at t = 7.51 h in a middle-layer of the depth (–28 m > z > –32 m) (d).

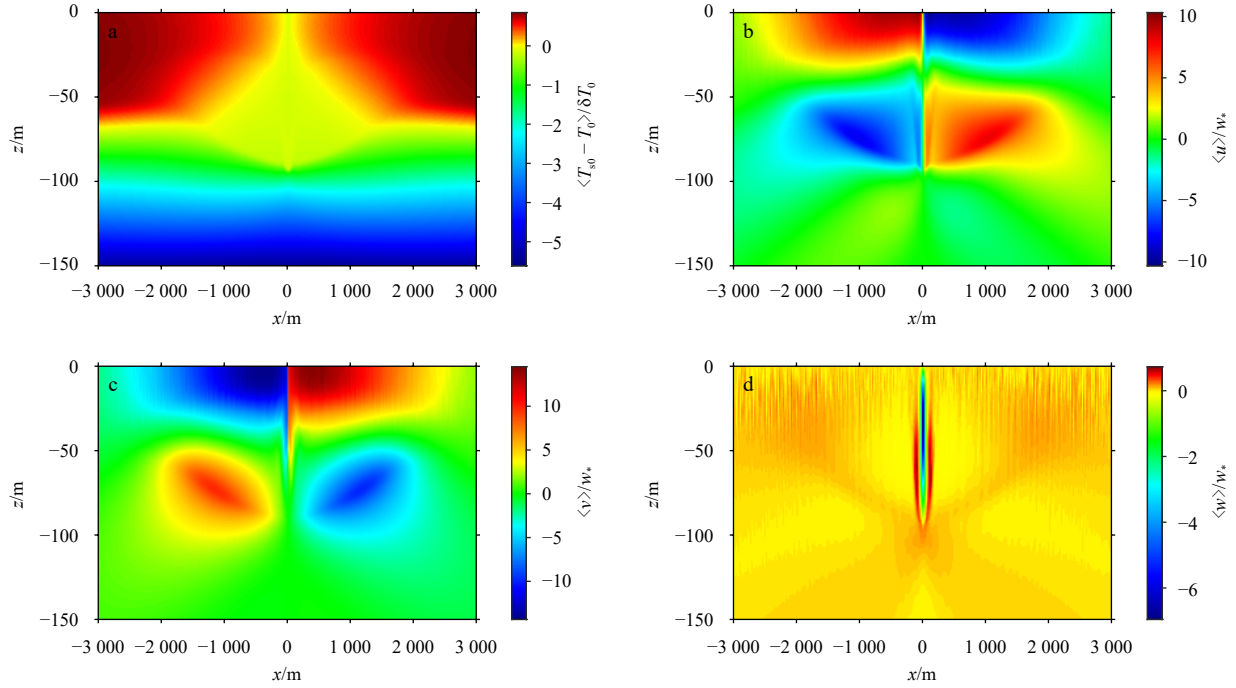

Fig. 4. Average submesoscale flow fields of the normalized temperature $\langle T_{s0} - T_0\rangle$ (a), the normalized cross-filament velocity $\langle u\rangle$ (b), the normalized down-filament velocity $\langle v\rangle$ (c), and the normalized velocity velocity $\langle w\rangle$ (d) at t = 3.27 h corresponding to the frontogenesis arrest.

responding to the time stamp of the first frontolysis arrest (Fig. 2). The width of cold filament above/below z = –22 m at t = 7.51 h (Fig. 5a) is wider/narrower relative to that at t = 3.27 h (Fig. 4a). This is owing to that the direction of the secondary circulations $\langle u, w\rangle$ at t = 7.51 h (Figs 5b and d) is opposite to that at t = 3.27 h (Figs 4b and d). Hence, the secondary circulations (Figs 4b and d) cause the cold/warm water flowing away from/toward the cold core above/below z = –22 m (Fig. 5b) and the upwelling jet in the range of the cold core transporting the cold water to the shallower depth (Fig. 5d). The negative/positive down-filament velocity

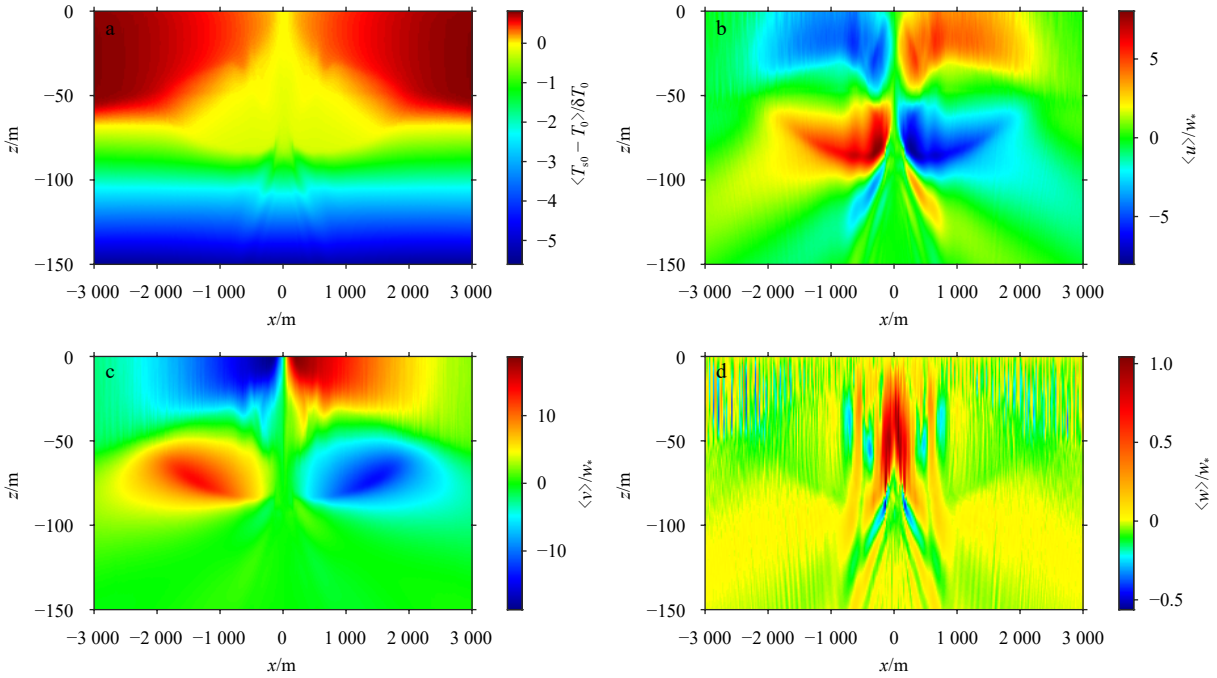

Fig. 5. Average submesoscale flow fields of the normalized temperature $\langle T_{s0} - T_0 \rangle$ (a), the normalized cross-filament velocity $\langle u \rangle$ (b), the normalized down-filament velocity $\langle v \rangle$ (c), and the normalized velocity $\langle w \rangle$ (d) at t = 7.51 h corresponding to the frontolysis arrest.

locates in the left/right flank of cold filament at t = 7.51 h (Fig. 5c), which is consistent with that at t = 3.27 h (Fig. 4c). This result indicates that the direction of the down-filament currents is not impacted by the inertial oscillation (Li et al., 2024). Moreover, the clear downwelling currents appear near the left and right edge of the upwelling jet, then the downwelling currents will gradually develop into the downwelling jet in the range of cold.

The change in the direction of the secondary circulations (Figs 4b and d and Figs 5b and d) can induce the conversion between the frontogenesis and the frontolysis of the cold filament (Figs 4a and 5a). In addition, the direction of the down-filament velocity is unchanged with time, which is due to that, for a cold filament, the direction of the down-filament currents is dominated by the horizontal temperature (buoyancy) gradient. The results suggest that the direction of the cross-filament secondary circulations is only changed by the Coriolis force, while the direction of the down-filament velocity does not be changed by Coriolis force. Furthermore, Figs 5a and d show that the water from the thermocline may be transported into the upper mixed layer, which should play an important role in the biochemical process.

3.3 *Evolution of submesoscale flow fields*

The evolution of the temperature and flow fields can directly display the frontogenesis processes of the cold filament caused by the thermal convection turbulence with time (McWilliams et al., 2015; Sullivan and McWilliams, 2018; Li et al., 2024). Figure 6 shows the variation of the submesoscale flow fields with time. The change in the direction of the secondary circulations $\langle u, w \rangle$ is periodic with time and the corresponding period is the inertial period ($2\pi/f$ = 14 h) (Figs 6b and d). The reason is that when the secondary circulations is activated by the vertical momentum flux, the magnitude and direction of the secondary circulations must be directly modulated by the Coriolis effect with time. The periodic change in the direction of the secondary circulations (Figs 6b and d) cases the periodic reduction and enlargement of the cold filament $\langle T_{s0} - T_0 \rangle$ in a near-surface layer of depth (0 m > z > –5 m) (Fig. 6a). This result suggests that the cold filament frontogenesis created by thermal convection turbulence includes both of the frontogenesis and the frontolysis. The magnitude of the down-filament velocity $\langle v \rangle$ in a near-surface layer of depth (0 m > z > –5 m) periodically varies with time, whereas the direction of the down-filament velocity is unchanged with time (Fig. 6c). This result further demonstrates that the Coriolis force only changes the magnitude of the down-filament velocity with time, but cannot change the direction of the down-filament velocity.

The intensity of the submesoscale currents with the surface horizontal convergence and the downwelling in the range of cold core is much stronger than that with the surface horizontal divergence and the upwelling (Figs 6b and d), which induces that cold filament frontogenesis is more intense relative to cold filament frontolysis (Fig. 6a). In addition to the periodic variation of the submesoscale currents, the total tendency of the intensity of the submesoscale currents becomes weak with time (Figs 6b, c and d), which is induced by the weakening temperature gradient (Fig. 6a) due to the turbulent mixing of the thermal convective turbulence and the submesoscale turbulence (McWilliams et al., 2005; Sullivan and McWilliams, 2018; Li et al., 2024). In addition, the width of the cold core gradually increases (Fig. 6a) with the reduction in the intensity of the secondary circulation (Figs 6b and d). This result implies that the final collapse of the cold filament may be through the turbulent mixing.

The evolution of the temperature field and secondary circulations in the vertical (z) direction with time is also the important information for parameterizing the influence of the cold filament frontogenesis on the large-scale motions in OGCMs, because which may further demonstrate the impact of the submesoscale frontogenesis and frontolysis on the variation of the upper mixed layer (Haney et al., 2015). The evolution of the secondary circulations $\langle u, w \rangle$ is that the cross-filament currents flowing toward/away from the filament center (Figs 7b and d) above/below z =

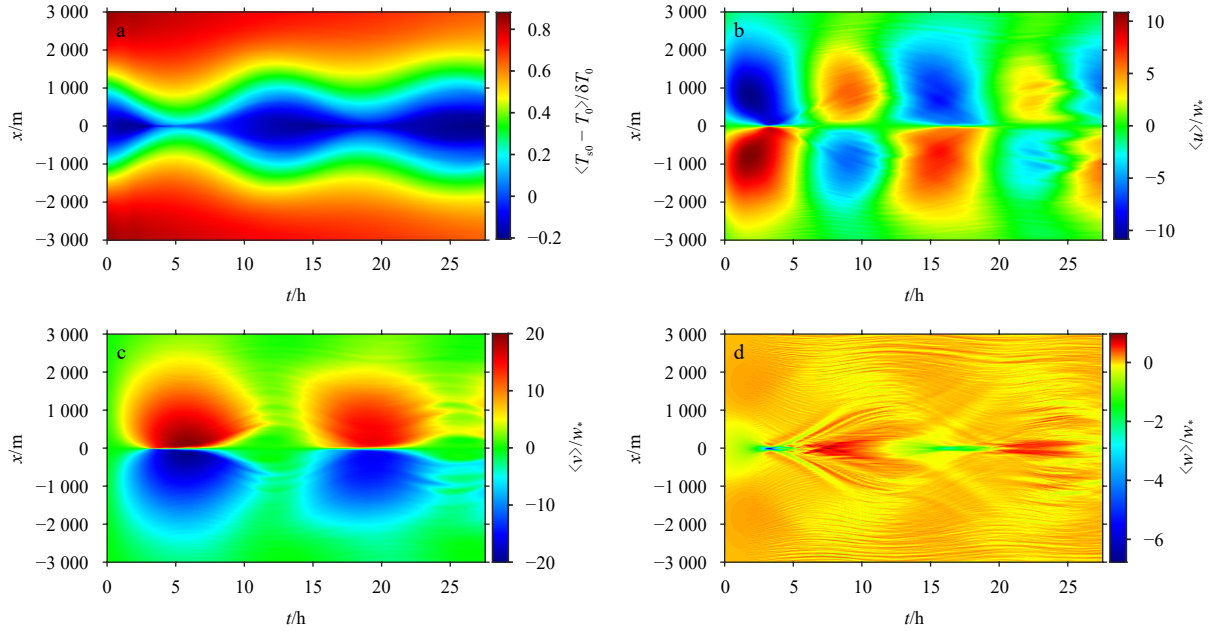

Fig. 6. The time variation of the submesoscale flow fields in the cross-filament (x) direction for the normalized temperature field $\langle T_{s0} - T_0\rangle$ in a near-surface layer (0 m > z > –5 m) (a), the normalized cross-filament current $\langle u\rangle$ in a near-surface layer (0 m > z > –5 m) (b), the normalized down-filament current $\langle v\rangle$ in a near-surface layer (0 m > z > –5 m) (c), and the normalized vertical current $\langle w\rangle$ (d) in the middle of the upper mixed layer (–28 m > z > –32 m).

–40 m with the downwelling jet (Fig. 7c) during the first half inertial period is changed into the cross-filament currents flowing away from/toward the filament center above/below z = –40 m (Figs 7b and d) with the upwelling jet (Fig. 7c) during the secondary half inertial period. The change in the direction of secondary circulations (Figs 7b, c, and d) induces the increase and decrease in the depth of the upper mixed layer and the enhancement and reduction in the stratification within the upper mixed layer in the filament center (x = 0) (Fig. 7a).

The tendency in the intensity of the secondary circulations becomes weak with time (Figs 7b, c and d), which causes the reduction in the variations of the upper mixed layer depth and the stratification within the upper mixed layer (Fig. 7a). This result indicates that the turbulent mixing of the thermal convective turbulence and the submesoscale turbulence (Sullivan and McWilliams, 2018, 2019) gradually reduces the intensity of the cold fila-

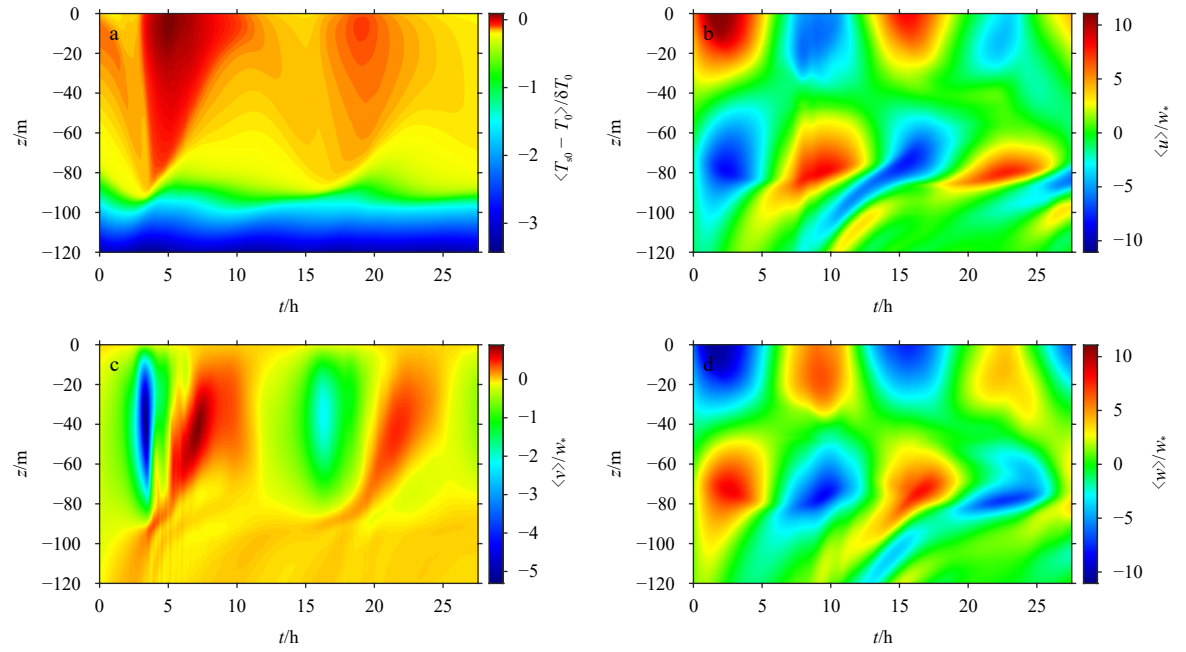

Fig. 7. The time variation of the submesoscale flow fields in the vertical (z) direction for the normalized temperature field $\langle T_{s0} - T_0\rangle$ at x = 0 that is averaged over –5 m < x < 5 m (a), the normalized cross-filament current $\langle u\rangle$ at x = –1 000 m that is averaged over –995 m > x > –1 005 m (b), the normalized vertical current $\langle w\rangle$ in a at x = 0 m that is averaged over 5 m > x > –5 m (c), and the normalized cross-filament current $\langle u\rangle$ at x = 1 000 m that is averaged over 1 005 m > x > 995 m (d).

ment frontogenesis and frontolysis with time (Fig. 7). Hence, this result further shows that the parametrization of the cold filament lifecycle should include the change in the depth of the upper mixed layer and the stratification within the upper mixed layer owing to the conversion between the frontogenesis the and frontolysis.

4 Summary

The frontogenesis process of the submesoscale cold filament caused by the thermal convection turbulence is studied by a nonhydrostatic large eddy simulation model. The results indicate that the change in the direction of the cross-filament secondary circulations is caused the inertial oscillation associated with the Coriolis force, suggesting that the magnitude and direction of the secondary circulations may be directly modulated by the Coriolis effect. Hence, the change in the direction of the secondary circulations causes the conversion between the frontogenesis and the frontolysis of the cold filament within an inertial period. The frontogenesis and frontolysis of the cold filament further induce the increase and decrease in the depth of the upper mixed layer and the enhancement and reduction in the stratification within the upper mixed layer. In addition, the width of the cold core gradually increases with the weakening intensity of the secondary circulations, which suggests that the final collapsion of the cold filament may be caused by turbulent mixing.

For a cold filament, the frontolysis is the reverse process of the frontogenesis. The direction of the secondary circulations for the cold filament frontolysis is opposite to that for the cold filament frontogenesis. Hence, during the frontolysis process, the secondary circulations may transport the nutrient rich water of the thermocline into the upper mixed layer, which plays an important role in the primary productivity of the ocean.

The parameterization schemes of the submesoscale front/filament processes only include the frontogenesis process in the present stage (Zhang et al., 2023b; Bodner et al., 2020, 2023). The conversion between the frontogenesis and frontolysis may periodically break and restore the structure of cold filament in this simulation, therefore the parameterization schemes of submesoscale front/filament processes needs to include the frontolysis process in the future.

Acknowledgements

This research was also supported by the Postdoctoral Innovation Practice Base of Hezhou University and the Guangxi Yuchai New Energy Co. Ltd. The large eddy simulation model is provided by the National Center for Atmospheric Research.

References

Barkan R, Molemaker M J, Srinivasan K, et al. 2019. The role of horizontal divergence in submesoscale frontogenesis. Journal of Physical Oceanography, 49(6): 1593–1618, doi: 10.1175/JPO-D-18-0162.1

Blumen W. 2000. Inertial oscillations and frontogenesis in a zero potential vorticity model. Journal of Physical Oceanography, 30(1): 31–39, doi: 10.1175/1520-0485(2000)030<0031:IOAFIA>2.0.CO;2

Bodner A S, Fox-Kemper B, Johnson L, et al. 2023. Modifying the mixed layer eddy parameterization to include frontogenesis arrest by boundary layer turbulence. Journal of Physical Oceanography, 53(1): 323–339, doi: 10.1175/JPO-D-21-0297.1

Bodner A S, Fox-Kemper B, Van Roekel L P, et al. 2020. A perturbation approach to understanding the effects of turbulence on frontogenesis. Journal of Fluid Mechanics, 883: A25

Boccaletti G, Ferrari R, Fox-Kemper B. 2007. Mixed layer instabilities and restratification. Journal of Physical Oceanography, 37(9): 2228–2250, doi: 10.1175/JPO3101.1

Capet X, McWilliams J C, Molemaker M J, et al. 2008a. Mesoscale to submesoscale transition in the California current system. Part I: Flow structure, eddy flux, and observational tests. Journal of Physical Oceanography, 38(1): 29–43, doi: 10.1175/2007JPO3671.1

Capet X, McWilliams J C, Molemaker M J, et al. 2008b. Mesoscale to submesoscale transition in the California current system. Part II: Frontal processes. Journal of Physical Oceanography, 38(1): 44–64, doi: 10.1175/2007JPO3672.1

Capet X, McWilliams J C, Molemaker M J, et al. 2008c. Mesoscale to submesoscale transition in the California current system. Part III: Energy balance and flux. Journal of Physical Oceanography, 38(10): 2256–2268, doi: 10.1175/2008JPO3810.1

Crowe M N, Taylor J R. 2018. The evolution of a front in turbulent thermal wind balance. Part 1. Theory. Journal of Fluid Mechanics, 850: 179–211, doi: 10.1017/jfm.2018.448

Crowe M N, Taylor J R. 2019. The evolution of a front in turbulent thermal wind balance. Part 2. Numerical simulations. Journal of Fluid Mechanics, 880: 326–352, doi: 10.1017/jfm.2019.688

Dauhajre D P, McWilliams J C, Uchiyama Y. 2017. Submesoscale coherent structures on the continental shelf. Journal of Physical Oceanography, 47(12): 2949–2976, doi: 10.1175/JPO-D-16-0270.1

Deardorff J W. 1972. Numerical investigation of neutral and unstable planetary boundary layers. Journal of the Atmospheric Sciences, 29(1): 91–115, doi: 10.1175/1520-0469(1972)029<0091:NIONAU>2.0.CO;2

Fox-Kemper B, Ferrari R, Hallberg R. 2008. Parameterization of mixed layer eddies. Part I: Theory and diagnosis. Journal of Physical Oceanography, 38(6): 1145–1165, doi: 10.1175/2007JPO3792.1

Gula J T, Molemaker M J, McWilliams J C. 2014. Submesoscale cold filaments in the Gulf Stream. Journal of Physical Oceanography, 44(10): 2617–2643, doi: 10.1175/JPO-D-14-0029.1

Hamlington P E, Van Roekel L P, Fox-Kemper B, et al. 2014. Langmuir-submesoscale interactions: Descriptive analysis of multiscale frontal spindown simulations. Journal of Physical Oceanography, 44(9): 2249–2272, doi: 10.1175/JPO-D-13-0139.1

Haney S, Fox-Kemper B, Julien K, et al. 2015. Symmetric and geostrophic instabilities in the wave-forced ocean mixed layer. Journal of Physical Oceanography, 45(12): 3033–3056, doi: 10.1175/JPO-D-15-0044.1

Hoskins B J. 1982. The mathematical theory of frontogenesis. Annual Review of Fluid Mechanics, 14: 131–151, doi: 10.1146/annurev.fl.14.010182.001023

Hypolite D, Romero L, McWilliams J C, et al. 2021. Surface gravity wave effects on submesoscale currents in the open ocean. Journal of Physical Oceanography, 51(11): 3365–3383

Kaminski A K, Smyth W D. 2019. Stratified shear instability in a field of pre-existing turbulence. Journal of Fluid Mechanics, 862: 639–658, doi: 10.1017/jfm.2018.973

Lapeyre G, Klein P, Hua B L. 2006. Oceanic restratification forced by surface frontogenesis. Journal of Physical Oceanography, 36(8): 1577–1590, doi: 10.1175/JPO2923.1

Leibovich S. 1983. The form and dynamics of Langmuir circulations. Annual Review of Fluid Mechanics, 15: 391–427, doi: 10.1146/annurev.fl.15.010183.002135

Li Guojing, Wang Dongxiao, Dong Changming, et al. 2024. Frontogenesis and frontolysis of a cold filament driven by the cross-filament wind and wave fields simulated by a large eddy simulation. Advances in Atmospheric Sciences, 41(3): 509–528, doi: 10.1007/s00376-023-3037-2

McWilliams J C. 2016. Submesoscale currents in the ocean. Proceedings of the Royal Society A: Mathematical, Physical, and Engineering Sciences, 472(2189): 20160117

McWilliams J C. 2017. Submesoscale surface fronts and filaments: secondary circulation, buoyancy flux, and frontogenesis. Journal of Fluid Mechanics, 823: 391–432, doi: 10.1017/jfm.2017.294

McWilliams J C. 2018. Surface wave effects on submesoscale fronts and filaments. Journal of Fluid Mechanics, 843: 479–517, doi: 10.1017/jfm.2018.158

McWilliams J C. 2019. A survey of submesoscale currents. Geoscience Letters, 6(1): 3, doi: 10.1186/s40562-019-0133-3
McWilliams J C. 2021. Oceanic frontogenesis. Annual Review of Marine Science, 13: 227–253, doi: 10.1146/annurev-marine-032320-120725
McWilliams J C, Colas F, Molemaker M J. 2009. Cold filamentary intensification and oceanic surface convergence lines. Geophysical Research Letters, 36(18): L18602, doi: 10.1029/2009GL039402
McWilliams J C, Fox-Kemper B. 2013. Oceanic wave-balanced surface fronts and filaments. Journal of Fluid Mechanics, 730: 464–490, doi: 10.1017/jfm.2013.348
McWilliams J C, Gula J, Molemaker M J, et al. 2015. Filament frontogenesis by boundary layer turbulence. Journal of Physical Oceanography, 45(8): 1988–2005, doi: 10.1175/JPO-D-14-0211.1
McWilliams J C, Sullivan P P, Moeng C H. 1997. Langmuir turbulence in the ocean. Journal of Fluid Mechanics, 334: 1–30, doi: 10.1017/S0022112096004375
Moeng C H. 1984. A large-eddy-simulation model for the study of planetary boundary-layer turbulence. Journal of the Atmospheric Sciences, 46(13): 2052–2062
Pham H T, Sarkar S. 2018. Ageostrophic secondary circulation at a submesoscale front and the formation of gravity currents. Journal of Physical Oceanography, 48(10): 2507–2529, doi: 10.1175/JPO-D-17-0271.1
Shakespeare C J, Taylor J R. 2013. A generalized mathematical model of geostrophic adjustment and frontogenesis: Uniform potential vorticity. Journal of Fluid Mechanics, 736: 366–413, doi: 10.1017/jfm.2013.526
Skyllingstad E D, Denbo D W. 1995. An ocean large-eddy simulation of Langmuir circulations and convection in the surface mixed layer. Journal of Geophysical Research: Oceans, 100(C5): 8501–8522, doi: 10.1029/94JC03202
Skyllingstad E D, Samelson R M. 2012. Baroclinic frontal instabilities and turbulent mixing in the surface boundary layer. Part I: Unforced simulations. Journal of Physical Oceanography, 42(10): 1701–1716, doi: 10.1175/JPO-D-10-05016.1
Smith K M, Hamlington P E, Fox-Kemmper B. 2016. Effects of submesoscale turbulence on ocean tracers. Journal of Geophysical Research: Oceans, 121(1): 908–933, doi: 10.1002/2015JC011089
Sullivan P P, McWilliams J C. 2018. Frontogenesis and frontal arrest of a dense filament in the oceanic surface boundary layer. Journal of Fluid Mechanics, 837: 341–380, doi: 10.1017/jfm.2017.833
Sullivan P P, McWilliams J C. 2019. Langmuir turbulence and filament frontogenesis in the oceanic surface boundary layer. Journal of Fluid Mechanics, 879: 512–553, doi: 10.1017/jfm.2019.655
Sullivan P P, McWilliams J C. 2024. Oceanic frontal turbulence. Journal of Physical Oceanography, 54(2): 333–358, doi: 10.1175/JPO-D-23-0033.1
Sullivan P P, McWilliams J C, Melville W K. 2007. Surface gravity wave effects in the oceanic boundary layer: Large-eddy simulation with vortex force and stochastic breakers. Journal of Fluid Mechanics, 593: 405–452, doi: 10.1017/S002211200700897X
Sullivan P P, McWilliams J C, Moeng C H. 1994. A subgrid-scale model for large-eddy simulation of planetary boundary-layer flows. Boundary-Layer Meteorology, 71(3): 247–276, doi: 10.1007/BF00713741
Sullivan P P, Patton E G. 2011. The effect of mesh resolution on convective boundary layer statistics and structures generated by large-eddy simulation. Journal of the Atmospheric Sciences, 68(10): 2395–2413, doi: 10.1175/JAS-D-10-05010.1
Suzuki N, Fox-Kemper B. 2016. Understanding stokes forces in the wave-averaged equations. Journal of Geophysical Research: Oceans, 121(5): 3579–3596, doi: 10.1002/2015JC011566
Taylor J R, Thompson A F. 2023. Submesoscale dynamics in the upper ocean. Annual Review of Fluid Mechanics, 55: 103–127, doi: 10.1146/annurev-fluid-031422-095147
Verma V, Pham H T, Sarkar S. 2019. The submesoscale, the finescale and their interaction at a mixed layer front. Ocean Modelling, 140: 101400, doi: 10.1016/j.ocemod.2019.05.004
Wang Dailin. 2011. Large-eddy simulation of the diurnal cycle of oceanic boundary layer: sensitivity to domain size and spatial resolution. Journal of Geophysical Research: Oceans, 106(C7): 13959–13974
Yuan Jianguo, Liang Junhong. 2021. Wind-and wave-driven ocean surface boundary layer in a frontal zone: Roles of submesoscale eddies and Ekman-Stokes transport. Journal of Physical Oceanography, 51(8): 2655–2680
Zhang Zhiwei, Liu Yuelin, Qiu Bo, et al. 2023a. Submesoscale inverse energy cascade enhances Southern Ocean eddy heat transport. Nature Communications, 14(1): 1335, doi: 10.1038/s41467-023-36991-2
Zhang Zhiwei, Zhang Xincheng, Qiu Bo, et al. 2021. Submesoscale currents in the subtropical upper ocean observed by long-term high-resolution mooring arrays. Journal of Physical Oceanography, 51(1): 187–206, doi: 10.1175/JPO-D-20-0100.1
Zhang Jinchao, Zhang Zhiwei, Qiu Bo. 2023b. Parameterizing submesoscale vertical buoyancy flux by simultaneously considering baroclinic instability and strain-induced frontogenesis. Geophysical Research Letters, 50(8): e2022GL102292, doi: 10.1029/2022GL102292